

CM² MAGAZINE



第 104 期



南方科技大学海洋磁学中心主编

<http://cm2.sustech.edu.cn/>

创刊词

海洋是生命的摇篮，是文明的纽带。地球上最早的生命诞生于海洋，海洋里的生命最终进化成了人类，人类的文化融合又通过海洋得以实现。人因海而兴。

人类对海洋的探索从未停止。从远古时代美丽的神话传说，到麦哲伦的全球航行，再到现代对大洋的科学钻探计划，海洋逐渐从人类敬畏崇拜幻想的精神寄托演变成可以开发利用与科学研究的客观存在。其中，上个世纪与太空探索同步发展的大洋科学钻探计划将人类对海洋的认知推向了崭新的纬度：深海（deep sea）与深时（deep time）。大洋钻探计划让人类知道，奔流不息的大海之下，埋藏的却是亿万年的地球历史。它们记录了地球板块的运动，从而使板块构造学说得到证实；它们记录了地球环境的演变，从而让古海洋学方兴未艾。

在探索海洋的悠久历史中，从大航海时代的导航，到大洋钻探计划中不可或缺的磁性地层学，磁学发挥了不可替代的作用。这不是偶然，因为从微观到宏观，磁性是最基本的物理属性之一，可以说，万物皆有磁性。基于课题组的学科背景和对海洋的理解，我们对海洋的探索以磁学为主要手段，海洋磁学中心因此而生。

海洋磁学中心，简称 CM^2 ，一为其全名“Centre for Marine Magnetism”的缩写，另者恰与爱因斯坦著名的质能方程 $E=MC^2$ 对称，借以表达我们对科学巨匠的敬仰和对科学的不懈追求。

然而科学从来不是单打独斗的产物。我们以磁学为研究海洋的主攻利器，但绝不仅限于磁学。凡与磁学相关的领域均是我们关注的重点。为了跟踪反映国内外地球科学特别是与磁学有关的地球科学领域的最新研究进展，海洋磁学中心特地主办 CM^2 Magazine，以期与各位地球科学工作者相互交流学习、合作共进！

“海洋孕育了生命，联通了世界，促进了发展”。21 世纪是海洋科学的时代，由陆向海，让我们携手迈进中国海洋科学的黄金时代。

目录

1. 快速小冰期是由于大西洋水入侵北欧海所致.....	1
2. 全球观测数据表明大气粉尘对高空卷云的形成起主导作用.....	4
3. 东赤道太平洋晚中新世-上新世早期的生物繁盛：来自 IODP U1335 孔的新见解.....	6
4. 南海东北缘晚中新世-第四纪地震地层学特征及其对构造和气候变化的响应	9
5. 来自西太平洋地区的水汽输送对孟加拉湾水汽同位素的作用.....	12
6. 气候突变与天文轨道理论：它们有联系吗?.....	14
7. 理解 ENSO 与北大西洋热带地区冬季 SST 变化之间的复杂关系.....	18
8. 约 30 Ma 以来青藏高原向其北缘的脉冲式隆起与生长.....	20
9. 火星放射性热形成的非岩浆水热系统.....	23
10. 青藏高原中部气候变化的轨道驱动揭示了晚渐新世至早中新世南亚季风的演化.....	25
11. 富营养和脱氧驱动 PETM 区间边缘海有机碳埋藏.....	27
12. 全球变暖扰动季风将使东亚气候由干转湿.....	31

1. 快速小冰期是由于大西洋水入侵北欧海所致

翻译人：仲义 zhongy@sustech.edu.cn



Francois L. and Raymond S B. Little Ice Age abruptly triggered by intrusion of Atlantic waters into the Nordic Seas [J] Science Advances, 2021, 7(51), eabi8230.

<https://www.science.org/doi/abs/10.1126/sciadv.abi8230>

摘要：小冰期（little Ice Age, LIG）是北半球后冰期时期最冷时期之一。尽管大量的证据表明该阶段形成与亚极地环流（subpolar gyre, SPG）减弱有关，但是导致其减弱状态的一系列事件尚未得到解释。本文，作者表明，小冰期的发生要超前于一次发生在 14 世纪晚期大西洋暖水入侵北欧海的事件。这次入侵是北大西洋上空大气持续阻塞所致，与异常高的太阳活动有关。温暖的海水导致了海冰的破裂和潮水冰川的崩解；14 世纪晚期大气阻塞异常使得大量的冰川聚集在北大西洋地区。进而导致亚极地环流的减弱，使得进入小冰期的时代。

ABSTRACT: The Little Ice Age (LIA) was one of the coldest periods of the postglacial period in the Northern Hemisphere. Although there is increasing evidence that this time interval was associated with weakening of the subpolar gyre (SPG), the sequence of events that led to its weakened state has yet to be explained. Here, we show that the LIA was preceded by an exceptional intrusion of warm Atlantic water into the Nordic Seas in the late 1300s. The intrusion was a consequence of persistent atmospheric blocking over the North Atlantic, linked to unusually high solar activity. The warmer water led to the breakup of sea ice and calving of tidewater glaciers; weakening of the blocking anomaly in the late 1300s allowed the large volume of ice that had accumulated to be exported into the North Atlantic. This led to a weakening of the SPG, setting the stage for the subsequent LIA.

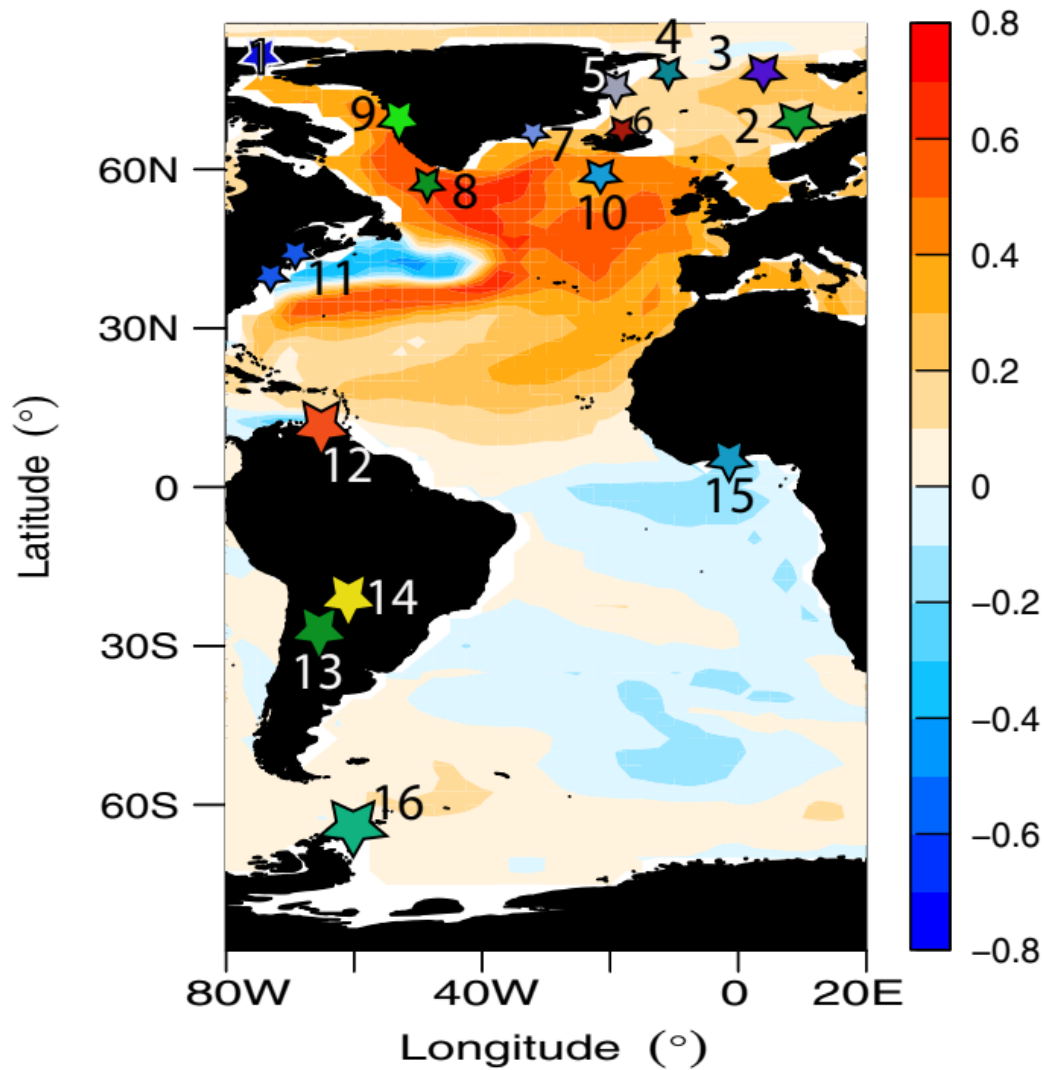


Figure 1. AMOC SST fingerprint. Multimodel mean correlation map between the low-frequency AMOC at 26°N and SST (12). Stars numbered 1 to 16 denote location of sites referred in the figures. The reconstructed AMV at South Sawtooth Lake (1), August temperature in Vøring Plateau off Norway (2), Eastern Fram Strait IRD (3), Atlantic water influence based on *C. neoterensis* in Western Fram Strait (4), East Greenland Strait *N. labradorica* (5), North Icelandic shelf temperature based on $\delta^{18}\text{O}$ from bivalve shells (6), IRD in Denmark Strait (7), the RAPiD-35-COM $\delta^{18}\text{O}$ *T. quinqueloba* (8), percentage of Atlantic species in Disko Bugt (9), the RAPID-21-COM sortable silt in the ISOW (10), Gulf of Maine reconstructed SST from bivalve shells (11), titanium (%) in the Cariaco Basin (12), Quelccaya ice record $\delta^{18}\text{O}$ (13), Huagapo speleothem $\delta^{18}\text{O}$ (14), and Lake Bosumtwi lake level inferred from $\delta^{18}\text{O}$ (15). The James Ross Island ice core record with annually resolved δD is shown (16).

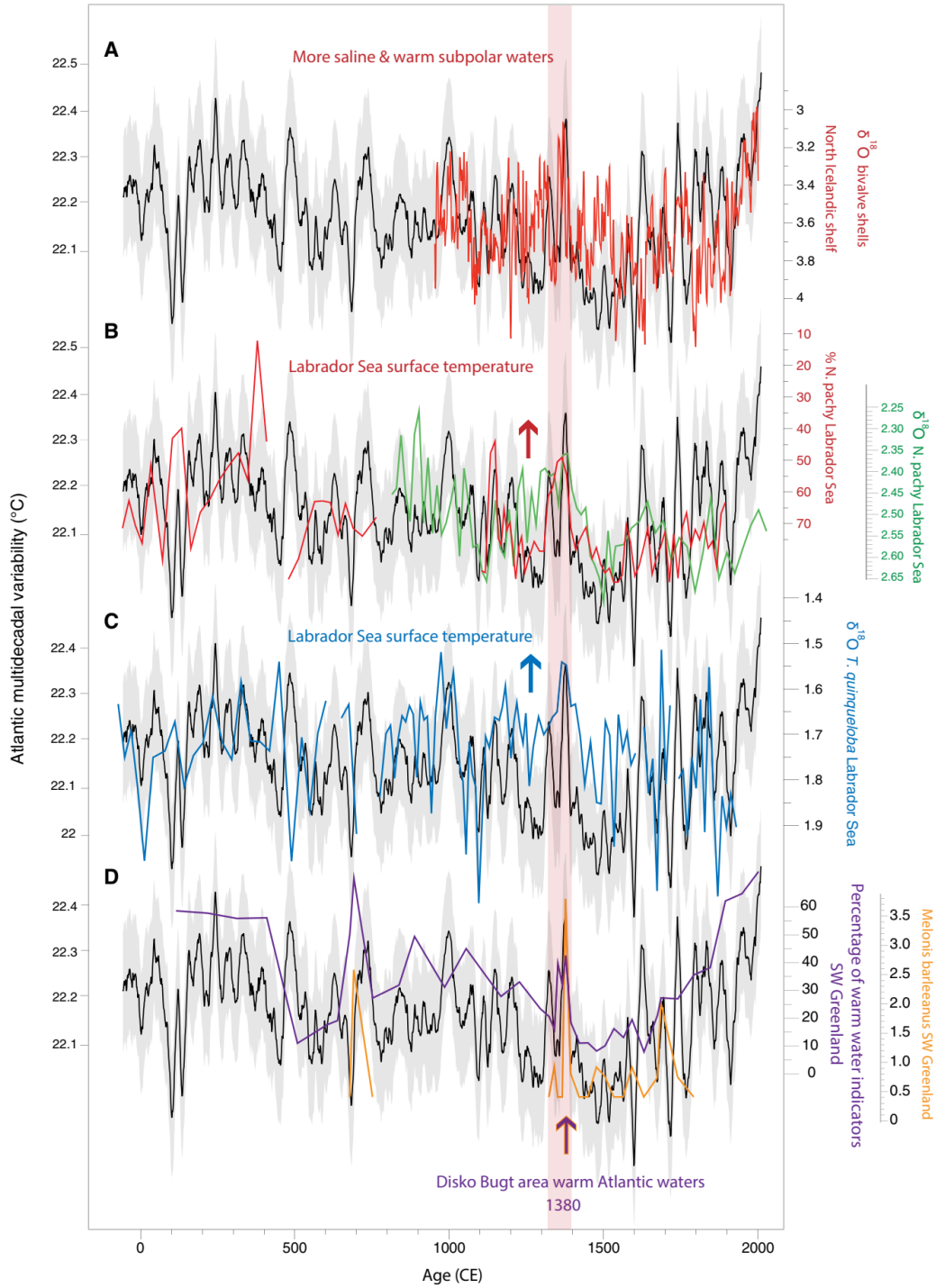


Figure 2. SPG SST anomalies in the past ~2000 years. (A) $\delta^{18}\text{O}$ of bivalve shells in the Iceland basin (33) shelf compared to the AMV. (B) Sea surface conditions in the Labrador Sea from $\delta^{18}\text{O}$ in *N. pachyderma* (red) in site RAPiD-35-COM (14) and green (18). (C) *T. quinqueloba* $\delta^{18}\text{O}$ from site RAPiD-35-25B at Eirik Drift (18). (D) Percentage of warm water indicators at Disko Bugt, South West (SW) Greenland with the individual Atlantic species *Melonis barleanus* (37).

2. 全球观测数据表明大气粉尘对高空卷云的形成起主导作用



翻译人：王敦繁 Dunfan-w@foxmail.com

Froyd K D, Yu P, Schill G P, et al. Dominant role of mineral dust in cirrus cloud formation revealed by global-scale measurement[J]. Nature Geoscience, 2022.

<https://doi.org/10.1038/s41561-022-00901-w>

摘要：空气中的粉尘颗粒可以作为对流层上部卷云的天然种子。然而，大气中大量的尘埃在形成卷云的区域是不受限制的，这妨碍了我们预测这些具有辐射重要性的云的能力。在这里，我们提供了对流层上层尘埃气溶胶丰度的全球尺度测量，并将这些数据纳入卷云形成的详细模型。我们发现，沙尘气溶胶在整个热带以外地区的所有季节都引发了卷云，并主导了北半球卷云的形成(季节性云的 75-93%)。我们还利用改进了的全球粉尘运输模型，探索了地球上哪些沙漠是向形成卷云区域输送灰尘气溶胶的最大贡献者。我们发现，每个排放区下游的气象环境调节了沙尘的大气寿命和输送到对流层上层的效率，使得沙尘源贡献与排放不成比例。我们的发现通过卷云的形成确立了粉尘在地球气候系统中的关键作用。

ABSTRACT: Airborne mineral dust particles can act as natural seeds for cirrus clouds in the upper troposphere. However, the atmospheric abundance of dust is unconstrained in cirrus-forming regions, hampering our ability to predict these radiatively important clouds. Here we present global-scale measurements of dust aerosol abundance in the upper troposphere and incorporate these into a detailed cirrus-formation model. We show that dust aerosol initiates cirrus clouds throughout the extra-tropics in all seasons and dominates cirrus formation in the Northern Hemisphere (75–93% of clouds seasonally). Using a global transport model with improved dust treatment, we also explore which of Earth’s deserts are the largest contributors of dust aerosol to cirrus-forming regions. We find that the meteorological environment downstream of each emission region modulates dust atmospheric lifetime and transport efficiency to the upper troposphere so that source contributions are disproportionate to emissions. Our findings establish the critical role of dust in Earth’s climate

system through the formation of cirrus clouds.

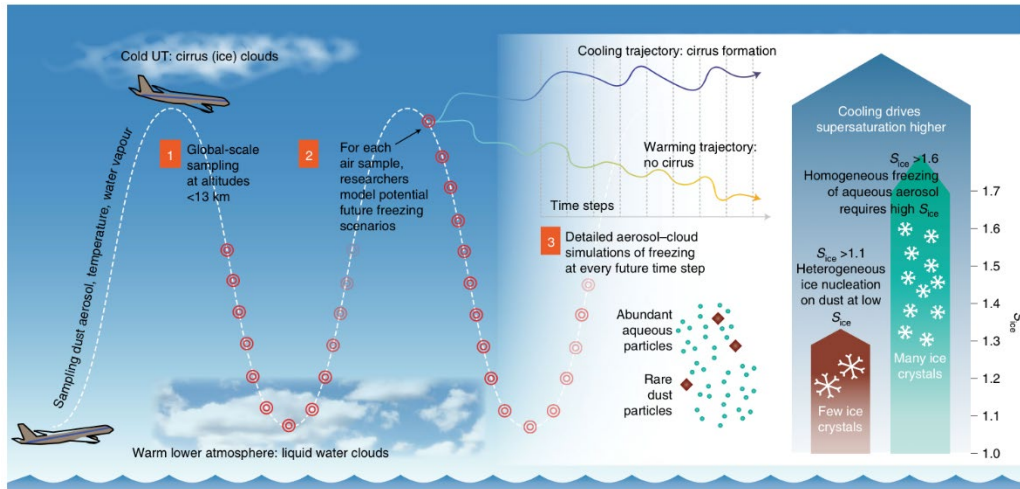


Figure 1. Predicting cirrus formation by combining in situ measurements with cloud–aerosol simulations. (1) Dust aerosol, water vapour and temperature are measured from aircraft during continuous vertical profiling, creating a global-scale map of initial conditions. (2) The future movement of each sampled air parcel is calculated from meteorological wind fields. Air parcels that ascend are cooled, whereby cirrus formation becomes possible. (3) Detailed microphysical simulations of cirrus formation are performed along each air parcel’s future trajectory to investigate the competition between dust heterogeneous nucleation and homogeneous freezing of background aqueous aerosol (Methods). S_{ice} denotes supersaturation of water vapour over ice. Credit: illustration by K. Bogan, CIRES, University of Colorado at Boulder.

3. 东赤道太平洋晚中新世-上新世早期的生物繁盛: 来自 IODP U1335 孔的新见解

翻译人: 王浩森 11930841@mail.sustech.edu.cn



Reghellin D, Coxall H K, Dickens G R, et al. *The late Miocene-early Pliocene biogenic bloom in the eastern equatorial Pacific: new insights from Integrated Ocean Drilling Program Site U1335[J]. Paleoclimatology and Paleoclimatology*, 2022, e2021PA004313.

<https://doi.org/10.1029/2021PA004313>

摘要: 中新世晚期-上新世早期的“生物繁盛”(BB)表现为沿赤道站位的生物源沉积大大增强,这与赤道东太平洋(EEP)较冷的海面温度(SST)有关。然而,EEP中BB的完整范围和几何形状尚不清楚。鉴于此,我们在位于赤道以北约5°和EEP以西的IODP站点U1335上,建立了7Ma以来新的碳酸盐含量(CaCO₃%)和碳酸盐稳定同位素($\delta^{13}\text{C}$ 和 $\delta^{18}\text{O}$)记录。U1335孔的 $\delta^{13}\text{C}$ 和 $\delta^{18}\text{O}$ 记录中高频变化与沉积物成分和物理性质的变化相耦合,能够与在更东的赤道范围所看到的模式相比较。在中新世晚期和上新世早期,与更东的两个赤道外站位相比,U1335的整体 $\delta^{18}\text{O}$ 更高,这表明更强的赤道上升流所产生的更冷的SST到达了现代上升流的西北部。在4.6Ma之前,相对较高的沉积速率也支持了U1335的上升流增强过程,这是BB期间较高生物产量的现象。这些观察结果表明,与今天相比,在BB期间,赤道上升流环流更集中,与赤道的平行度更低。

ABSTRACT: The late Miocene-early Pliocene “biogenic bloom” (BB) manifests as greatly enhanced biogenic sedimentation in sites along the Equator that has been linked to cooler sea surface temperature (SST) in the eastern equatorial Pacific (EEP). However, the full extent and geometry of the BB in the EEP is less known. To improve on this, we have generated new carbonate content (CaCO₃%) and bulk carbonate stable isotope ($\delta^{13}\text{C}$ and $\delta^{18}\text{O}$) records spanning the last 7 Ma at IODP Site U1335, located ca. 5° north of the Equator and to the west of the EEP. Site U1335 $\delta^{13}\text{C}$ and $\delta^{18}\text{O}$ records display high-frequency variations coupled to changes in sediment composition and physical properties comparable to patterns seen at on-Equator sites further east. During the late

Miocene and the early Pliocene bulk $\delta^{18}\text{O}$ is higher at Site U1335 compared to two off-Equator sites further east, suggesting cooler SSTs generated by stronger equatorial upwelling reaching northwest of the modern core-equatorial upwelling belt. Enhanced upwelling at Site U1335 is supported by relatively higher sedimentation rates prior to 4.6 Ma, symptomatic of higher biological production during the BB. These observations suggest that during the BB the equatorial upwelling circulation was more focused and less parallel to the Equator compared to present day.

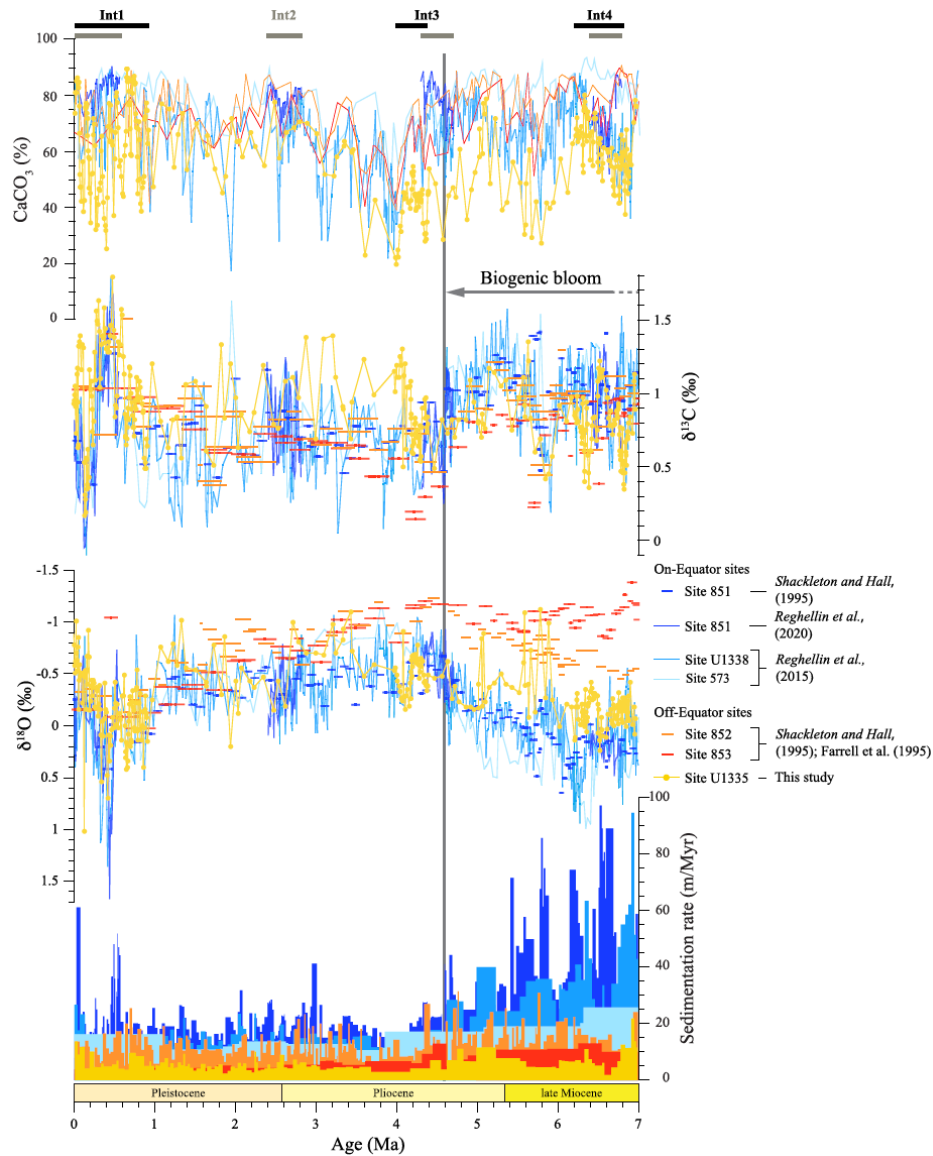


Figure 1. Comparison between relevant published CaCO₃%, bulk carbonate $\delta^{13}\text{C}$ and $\delta^{18}\text{O}$ and sedimentation rate records from the eastern equatorial Pacific (EEP) for the last 7 Ma at Site 851 with new data from Site U1335 (this study). The vertical gray line represents the end of the biogenic bloom (BB; ca. 4.6 Ma) as suggested by geochemical records at sites examined in this study. Ages for samples at Sites U1335 and U1338 were determined using the age model of Lyle et al. (2019).

Note that Site U1335 $\delta^{18}\text{O}$ displays much similar values compared to on-Equator sites than off-Equator sites, suggesting BB conditions at site location. The low linear sedimentation rate (LSR) even during the BB is due to intense carbonate dissolution at Site U1335.

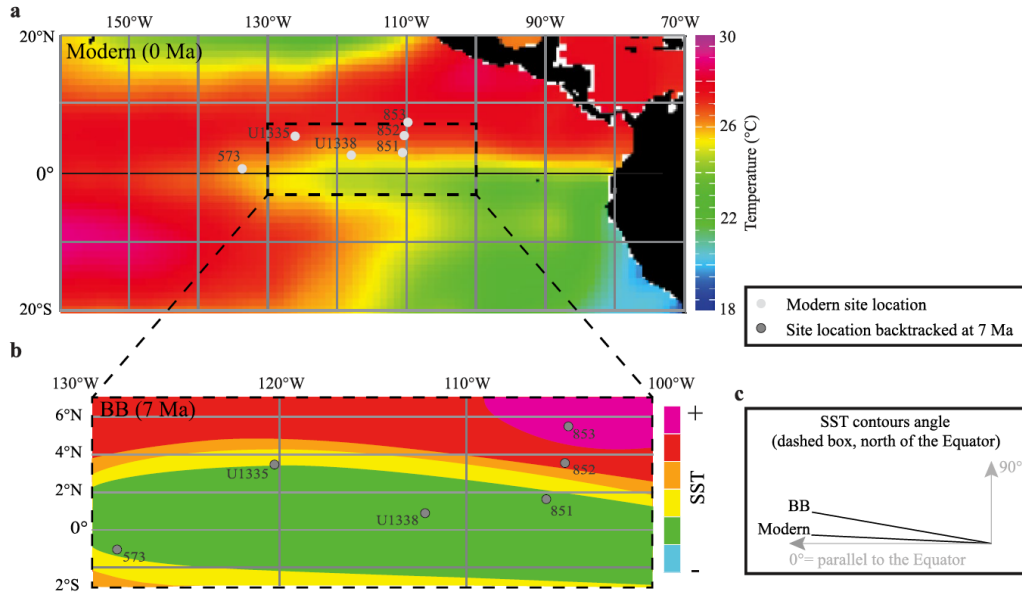


Figure 2. Comparison between the eastern equatorial Pacific (EEP) wind-driven equatorial upwelling system under modern and reconstructed biogenic bloom (BB) conditions. Modern average SST (a), qualitative SST gradients at 7 Ma inferred from bulk stable isotopes, $\text{CaCO}_3\%$ and linear sedimentation rate (LSR) at sites discussed in this study (b) and inclination of SST contours under modern and BB conditions (c). Given the large N-S gradients in surface water properties across the EEP, BB conditions reconstruction is restricted to the area adjacent to the backtracked location at 7 Ma of the sites examined, which roughly correspond to the Ocean area comprised between 3°S and 7°N latitude and between 100°W and 130°W longitude (dashed black box in panel a). The inclination angles of SST contours refer only to the area north of the Equator and within the dashed box. The BB was at its acme at about 7 Ma in the EEP as indicated by the bulk sediment proxies at multiple locations across the EEP. Note that during the BB meridional SST gradients were greater compared to present day as indicated by warmer SST at Sites 852 and 853. However, SST was cooler at Site U1335 compared to modern suggesting that equatorial upwelling circulation was less parallel to the Equator compared to modern, with SST contours moving northwards with increasing longitude.

4. 南海东北缘晚中新世-第四纪地震地层学特征及其对构造和气候变化的响应

翻译人: 刘伟 inewway@163.com



Wang X, Cai F, Sun Z, et al. *Late Miocene–Quaternary seismic stratigraphic responses to tectonic and climatic changes at the northeastern margin of the South China Sea [J]. GSA Bulletin, 2022.*
<https://doi.org/10.1130/B36224.1>

摘要: 构造和气候演化特征能在深水地层中有较好的记录。基于新获取的高分辨率二维多道地震剖面和多波束测深数据, 结合 ODP/IODP 数据, 研究了南海东北缘晚中新世-第四纪深水地震地层和沉积演化特征, 以及其对区域构造和气候变化的响应。晚中新世—第四纪地层自下而上可划分为 SU-1、SU-2 和 SU-3 三个单元, 其形成时间分别为 10.5~6.5 Ma (第 1 阶段)、6.5~0.9 Ma (第 2 阶段) 和 0.9 Ma - 现今 (第 3 阶段)。SU-1 以席状地震反射特征为主, 厚度变化不大, SU-2 和 SU-3 以丘状、透镜状、环槽 (moat) 等深积岩地震反射特征为主。这指示了第 1 阶段到第 2 阶段的底流增强, 可能是由于~6.5 Ma 以来吕宋岛弧与欧亚大陆构造碰撞影响下吕宋海峡附近的岩床抬升所致。SU-2 和 SU-3 的界面表现为全盆地范围的高振幅地震反射特征, 跨越这一界面, 平均沉积速率显示出从~28 m/m.y. (SU-2) 到 144 m /m.y. (SU-3) 的急剧增加。0.9 Ma 以来的高沉积物供给速率可能与中更新世气候转型有关, 这个时期降雨充沛, 促进了台湾造山带向南海供给了更多的沉积物。本文的研究表明, 南海东北缘深水地层记录了吕宋海峡附近的构造碰撞与中更新世气候转型事件, 对认识西太平洋最大边缘海盆地的构造、古气候、古海洋学和深水沉积过程有重要意义。

ABSTRACT: Tectonic and climate evolution could be well archived in deep-water stratigraphy. Based on newly acquired high-resolution two-dimensional (2-D) multichannel seismic profiles and multibeam bathymetry, together with Ocean Drilling Program/International Ocean Discovery Program (ODP/IODP) data, this study investigated the late Miocene–Quaternary deep-water seismic stratigraphy, sedimentary evolution, and responses to regional tectonic and climatic variations at the northeastern margin of the South China Sea. The late Miocene–Quaternary

stratigraphy consists of three units (i.e., SU-1, SU-2, and SU-3 from bottom to top) that are dated to 10.5–6.5 Ma (stage 1), 6.5–0.9 Ma (stage 2), and 0.9 Ma–present (stage 3), respectively. SU-1 is dominated by sheeted drifts with slight thickness variation, but SU-2 and SU-3 mainly consist of mounded, lenticular contourite drifts and channel-like moats. This suggests that the bottom currents intensified from stage 1 to stage 2, which was probably caused by the sill uplifting at the Luzon Strait under the influence of tectonic collision between the Luzon arc and Eurasia since ca. 6.5 Ma. SU-2 and SU-3 are separated by a basinwide high-amplitude seismic reflection, across which the average sedimentation rate shows a dramatic increase from ~28 m/m.y. in SU-2 to ~144 m/m.y. in SU-3. The high sediment supply since 0.9 Ma could be linked to the mid-Pleistocene climate transition, which resulted in abundant rainfall that promoted the Taiwan orogen to contribute more sediments to the South China Sea. This study indicates that the deep-water stratigraphy recorded the tectonic collision around the sole deep-water gateway (i.e., Luzon Strait) and mid-Pleistocene climate transition event at the northeastern South China Sea margin, which has important implications for understanding the relationships among the tectonic, paleoclimatic, paleoceanographic, and deep-water sedimentary processes in the largest marginal basin of the western Pacific Ocean.

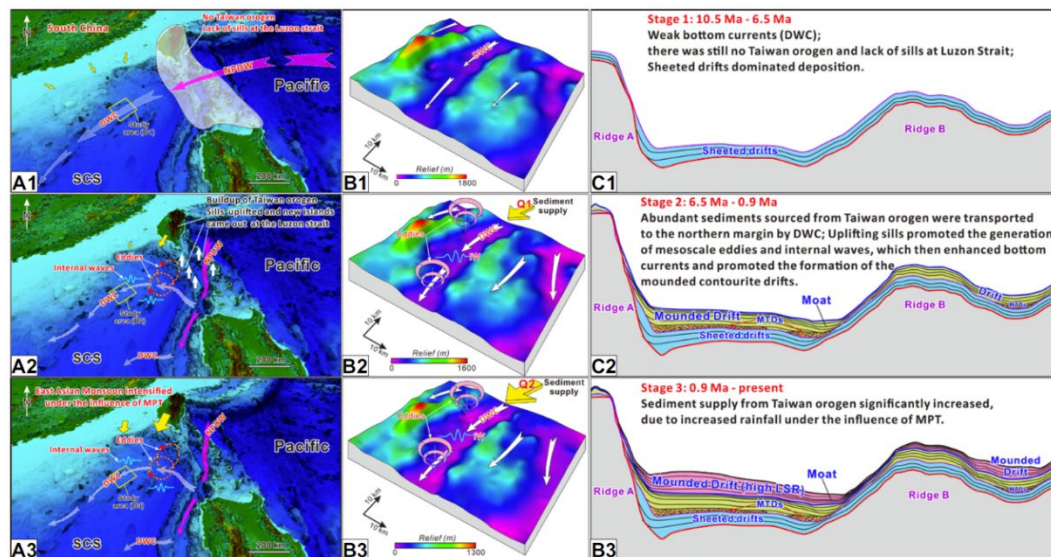


Figure 1. (A1–A3) Diagrams showing the inferred regional tectonic and paleoceanographic settings of the northeastern South China Sea (SCS) from stage 1 to stage 3. Magenta arrows represent the

North Pacific Deep Water (NPDW); transparent white arrows represent the Deep Water Current (DWC) circulation within the South China Sea; red-yellow dashed circle arrows in A2 and A3 indicate mesoscale eddies; cyan waves indicate internal waves; bold yellow arrows in A2 and A3 indicate the major sediment supply; and bold white arrows at Luzon Strait in A2 indicate the uplifting of sills. White transparent area in A1 indicates that there was no Taiwan orogen and lack of shallow-water sills and islands at the Luzon Strait during stage 1 (10.5–6.5 Ma), when the North Pacific Deep Water could intrude into the South China Sea freely and trigger little mesoscale eddies and internal waves. MPT—mid-Pleistocene climate transition. (B1–B3) Schematic diagrams illustrating the varying oceanographic dynamics and sediment supply over time. The mesoscale eddies (pink circles) and internal waves (IW; cyan waves) in B2 and B3 are labeled. The increased sediment supply in stage 3 is indicated by the bolder yellow arrows in B3. (C1–C3) Sketch of the stratigraphic architecture evolution over time. Note the transition from sheeted drifts within stage 1 to mounded drifts in stage 2, and the significant sedimentation rate increase from stage 2 to 3. LSR—linear sedimentation rate; MTDs—mass transport deposits; MPT—mid-Pleistocene.

5. 来自西太平洋地区的水汽输送对孟加拉湾水汽同位素的作用

翻译人: 杨会会 11849590@mail.sustech.edu.cn



Lekshmy P R, Midhun M, Ramesh R. *Role of moisture transport from Western Pacific region on water vapor isotopes over the Bay of Bengal [J]. Atmospheric Research, 2022, 265, 105895*

<https://doi.org/10.1016/j.atmosres.2021.105895>

摘要: 孟加拉湾 (BoB) 地区是印度夏季风 (ISM) 和周围地区东北季风 (NEM) 降雨的主要水汽来源。外围降水的氧同位素比值 ($\delta^{18}\text{O}$) 在 ISM 后期呈减小趋势, 在 NEM 期间最小。以前可以用 BoB 的局部因素来解释这一现象, 如同位素偏负的河流输入 BoB 地区、气旋活动增加等。然而, 确切的原因仍不清楚。在没有气旋活动的情况下, 从 BoB 收集的水汽 $\delta^{18}\text{O}$ 在 NEM 季节比 ISM 季节减少约 2‰。在本文中我们发现, 东风通过对流活跃的窄带 (赤道太平洋中部至西部和印度尼西亚地区), 将大量 (中位数 64%:四分位数范围 30%) 同位素偏负的水分带到 BoB 地区, 并导致 NEM 期间 BoB 上空的水汽异常负偏。来自 isotope enabled Community Atmospheric Model 模型的水汽源标记模拟结果显示, 从西太地区来的东风水汽流主导了 BoB 表层蒸发通量。

ABSTRACT: Bay of Bengal (BoB) region is a major moisture source to both Indian Summer Monsoon (ISM) and North East Monsoon (NEM) rainfall over the surrounding region. Oxygen isotopic ratios ($\delta^{18}\text{O}$) in the rainfall over the peripheral region show a decreasing trend towards the later months of ISM and shows minimum during NEM. This was previously explained with local factors of BoB such as isotopically depleted river discharge to BoB, increased cyclonic activity etc., however, the exact reasons remain unclear. $\delta^{18}\text{O}$ of vapor collected from BoB when there was no cyclonic activity also shows ~2‰ depletion in NEM season compared to that during ISM. Here we show, easterly winds passing through a convectively active narrow zonal band (central to western equatorial Pacific and Indonesian region) bring significant amounts (median 64%: interquartile range 30%) of isotopically depleted moisture to BoB region, and results in anomalous depletion of

vapor over BoB during NEM. Vapor source-tagged simulations from isotope enabled Community Atmospheric Model show easterly moisture flux from western Pacific region dominates over the BoB surface evaporation flux.

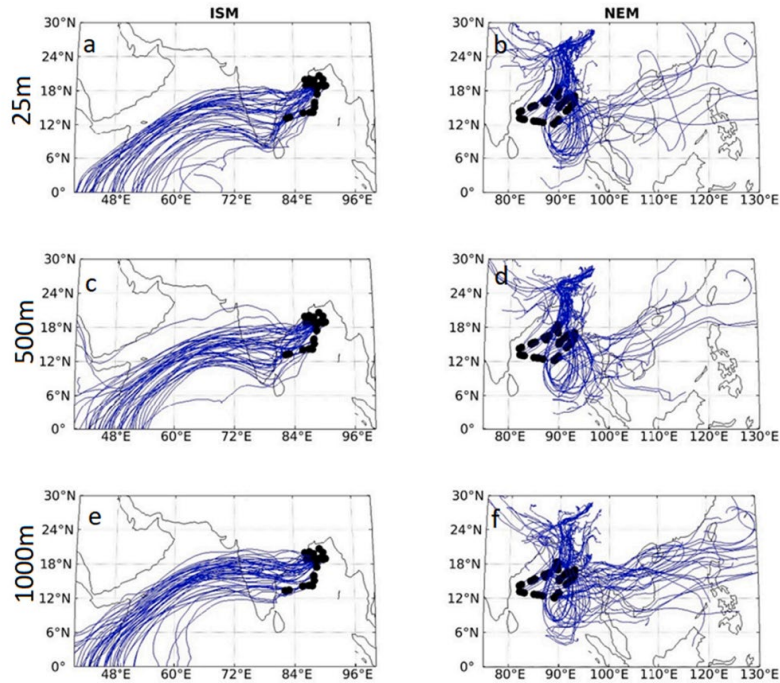


Figure 1. 240 h back trajectories generated at 25 m (a and b), 500 m(c and d) and 1000 m (e and f) above the mean sea level towards the sampling locations of ISM (left) and NEM (right) seasons.

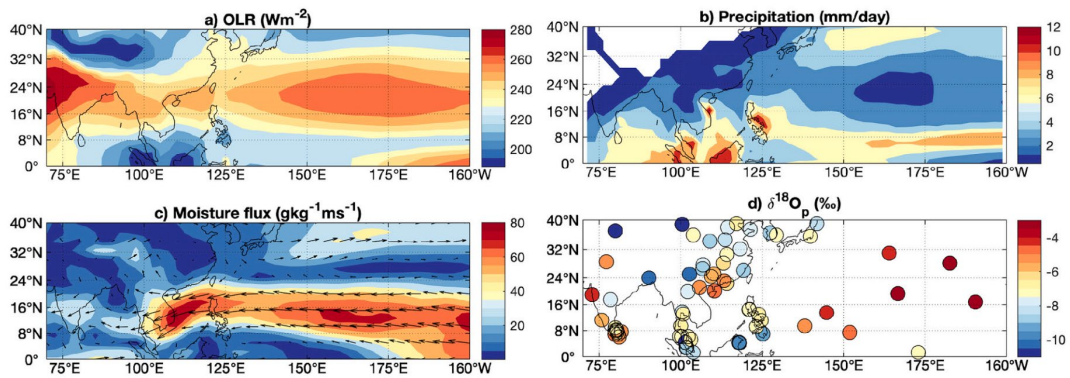


Figure 2. Climatological (1981-2010) average of a) OLR, b) precipitation and c) moisture flux (850 hPa) calculated for NEM season (October to December). d) is the same as others but for $\delta^{18}O_p$ for the period 1961-2014.

6. 气候突变与天文轨道理论：它们有联系吗？



翻译人：张亚南 zhangyn3@mail.sustech.edu.cn

Rousseau D-D, Bagniewski W, Ghil M. Abrupt climate changes and the astronomical theory: are they related? [J]. Climate of the Past, 2022,18,249-271.

<https://doi.org/10.5194/cp-18-249-2022>

摘要：突变气候是指十年到百年尺度或者千年尺度上所发生的突发性气候变化，其产生原因被认为涉及到气候系统内部过程的变化。相比之下，轨道强迫涉及到的气候变化则是受到气候系统之外的过程，其数千年的准周期变化在天文理论上的解释已经众所周知。文中，作者重新研究了北大西洋 U1308 孔记录的主要气候变化，覆盖了过去 3.2 Myr 详细的北半球冰盖崩解历史。U1308 钻孔记录中冰筏碎屑（IRD）事件的幅度和周期能够确定出几次突变气候发生的事件，其中以大规模的冰盖排放定义为 Heinrich events（HEs）。与此同时，在格陵兰岛末次冰期旋回中也记录到了被称为 Dansgaard Oeschger（DO）events 的突然变暖现象。结合 HE 和 DO 事件的记录，作者研究了记录中千年尺度变化的复杂机制，包括了过去 0.9 Myr 以来的气候突变。这一过程以 Bond 循环为特征，将 DO 事件与相关的 Greenland stadials 组合成一个逐渐变冷的趋势，其中每一个 stadials 都会发现 IRD 的记录，在循环的最后则是 HE。这种 Bond 循环可能在过去 0.9 Ma 都有发生，该时期内北半球冰盖达到最大范围和体积，因此成为该时期内气候变化的主要因素。由于第四纪时期冰盖变化与轨道变化同步，作者认为在中更新世和上新世记录的突变气候与天文轨道理论有着间接的联系。

ABSTRACT: Abrupt climate changes are defined as sudden climate changes that took place over tens to hundreds of years or recurred at millennial timescales; they are thought to involve processes that are internal to the climate system. By contrast, astronomically forced climate changes involve processes that are external to the climate system and whose multi-millennial quasi-periodic variations are well known from astronomical theory. In this paper, we re-examine the main climate variations determined from the U1308 North Atlantic marine record, which yields a detailed calving

history of the Northern Hemisphere ice sheets over the past 3.2 Myr. The magnitude and periodicity of the ice-rafted debris (IRD) events observed in the U1308 record allow one to determine the timing of several abrupt climate changes, the larger ones corresponding to the massive iceberg discharges labeled Heinrich events (HEs). In parallel, abrupt warmings, called Dansgaard–Oeschger (DO) events, have been identified in the Greenland records of the last glaciation cycle. Combining the HE and DO observations, we study a complex mechanism giving rise to the observed millennial-scale variability that subsumes the abrupt climate changes of last 0.9 Myr. This process is characterized by the presence of Bond cycles, which group DO events and the associated Greenland stadials into a trend of increased cooling, with IRD events embedded into every stadial, the latest of these being an HE. These Bond cycles may have occurred during the last 0.9 Ma when Northern Hemisphere ice sheets reached their maximum extent and volume, thus becoming a major player in this time interval's climate dynamics. Since the waxing and waning of ice sheets during the Quaternary period are orbitally paced, we conclude that the abrupt climate changes observed during the Middle Pleistocene and Upper Pleistocene are therewith indirectly linked to the astronomical theory of climate.

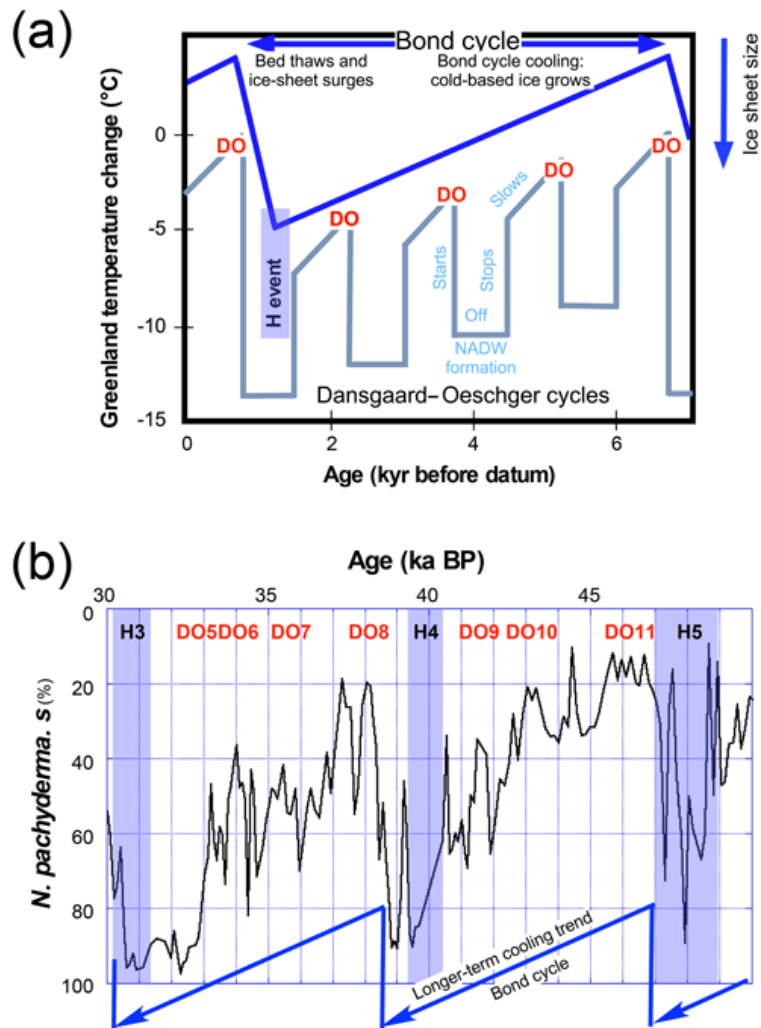


Figure 1. Description of a Bond cycle. (a) Idealized Bond cycle as illustrated following Alley (1998). DO stands for Dansgaard–Oeschger event, H event stands for Heinrich event, and NADW stands for North Atlantic Deep Water. (b) Variations in the percentage of *Neogloboquadrina pachyderma* (s.), a species indicative of cold surface water, from DSDP 609 (Bond et al., 1992), illustrating two Bond cycles. These cycles show a series of Dansgaard–Oeschger (DO) cycles composed of an abrupt warming that is followed by a return to glacial conditions represented by “stadials”. Every Bond cycle corresponds to a long-term cooling trend that starts with a strong warming and ends with a stadial that includes a massive iceberg discharge into the North Atlantic; Heinrich events are marked by a letter “H” followed by a number assigned by Bond et al. (1992).

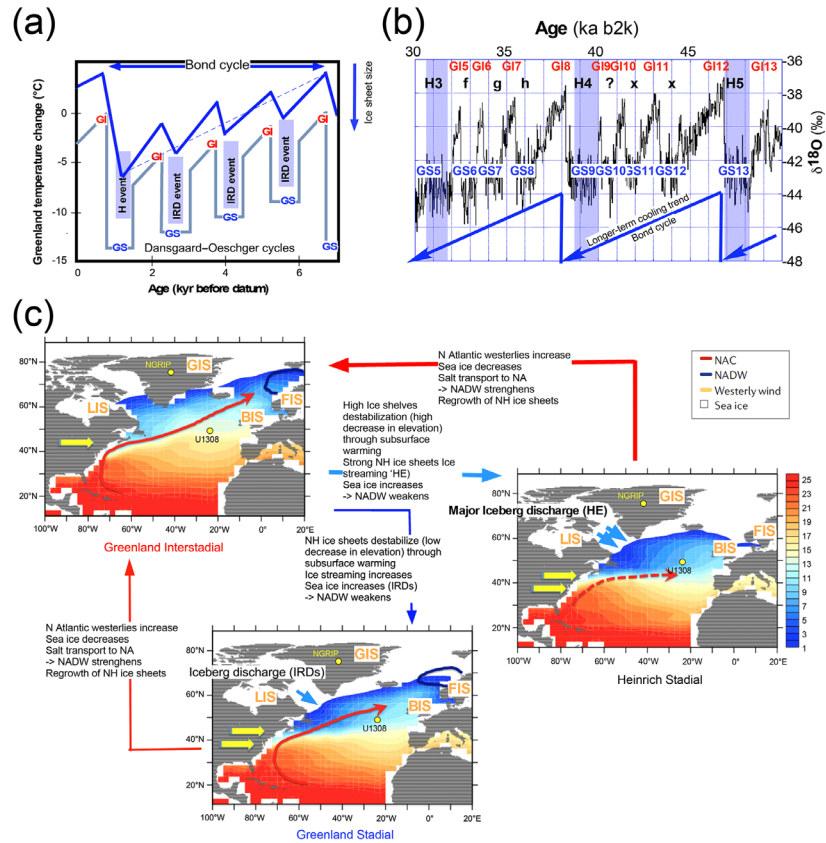


Figure 2. Schematic diagram of the proposed updated Bond cycle. (a) The amended scheme here differs from the one in Fig. 6a by adding the IRD event associated to every Greenland stadials (GS). The canonical DO are labeled here Greenland interstadials (GI). (b) The revised cycle here differs from the one in Fig. 1a by using the NGRIP $\delta^{18}\text{O}$ data (Rasmussen et al., 2014) to mark the GSs and GIs. IRD events observed in contemporaneous marine records by Bond and Lotti (1995), are indicated by the letters “f” to “h”, while IRD events that were observed but not assigned a number also by Bond and Lotti (1995), are indicated by a letter “x”. HE numbers are the same as in Fig. 5. (c) Maps illustrating the climate evolution associated with the “long-term cooling trend” that corresponds to a Bond cycle in panel (a). The last DO cycle, named a Heinrich stadial, is characterized by a massive release of icebergs. Annual mean sea surface temperature ($^{\circ}\text{C}$) for a GI (here 47 ka), a GS (here 44.4 ka), and a Heinrich stadial (at 48 ka), as simulated in a transient experiment of MIS3 (Menviel et al., 2014, 2021). GIS stands for Greenland ice sheet, LIS stands for Laurentide ice sheet, BIS stands for British Isles ice sheet, and FIS stands for Fennoscandian ice sheet.

7. 理解 ENSO 与北大西洋热带地区冬季 SST 变化之间的复杂关系

翻译人: 李海 12031330@mail.sustech.edu.cn



Jiang F, Zhang W. Understanding the complicated relationship between ENSO and wintertime North Tropical Atlantic SST variability [J]. Geophysical Research Letters, 2022, 49, e2022GL097889

<https://doi.org/10.1029/2022GL097889>

摘要: 厄尔尼诺-南方涛动 (ENSO) 在其减弱的春季可能会影响北大西洋热带地区 (NTA) 的海表温度 (SST), 为 NTA 的可预测性提供了重要来源。然而, 北大西洋热带地区的 SST 与 ENSO 在冬季没有呈现正相关的关系, 阻碍了对冬季北大西洋热带地区 SST 波动的准确预测。作者发现这一现象主要是由于 NTA 的先决条件不同。以前一个夏季 NTA 的 SST 状态作为初始条件, 建立了 ENSO 与冬季 NTA 海表温度变化之间的稳健关系。此外, 作者发现 NTA 的初始条件部分可追溯到 ENSO 的先决条件。同时, 局部大气条件在塑造 NTA 的 SST 变化中发挥作用, 尤其是厄尔尼诺事件在夏季的发展。理解 ENSO 与冬季 NTA 的 SST 变化之间的复杂关系对探讨跨流域气候相互作用和相关气候可预测性具有重要意义。

ABSTRACT: The El Niño-Southern Oscillation (ENSO) is known to influence the North Tropical Atlantic (NTA) sea surface temperature (SST) during its decaying spring, providing an essential source of NTA predictability. However, the positive ENSO–NTA SST relationship is absent during boreal winter, impeding accurate anticipation of wintertime NTA SST fluctuations. We find that this absence is mainly due to different NTA preconditions. Taking into account the previous summer NTA SST state as an initial condition, a robust relationship is established between ENSO and wintertime NTA SST variability. Furthermore, we show that the NTA initial conditions are in part traced to the ENSO preconditions. Besides, the simultaneous local atmospheric conditions play a role in shaping the initial NTA SST variabilities, especially in the developing summer of El Niño events. The understanding of the complicated ENSO–wintertime NTA SST relationship has implications for exploring trans-basin climate interactions and associated climate predictability.

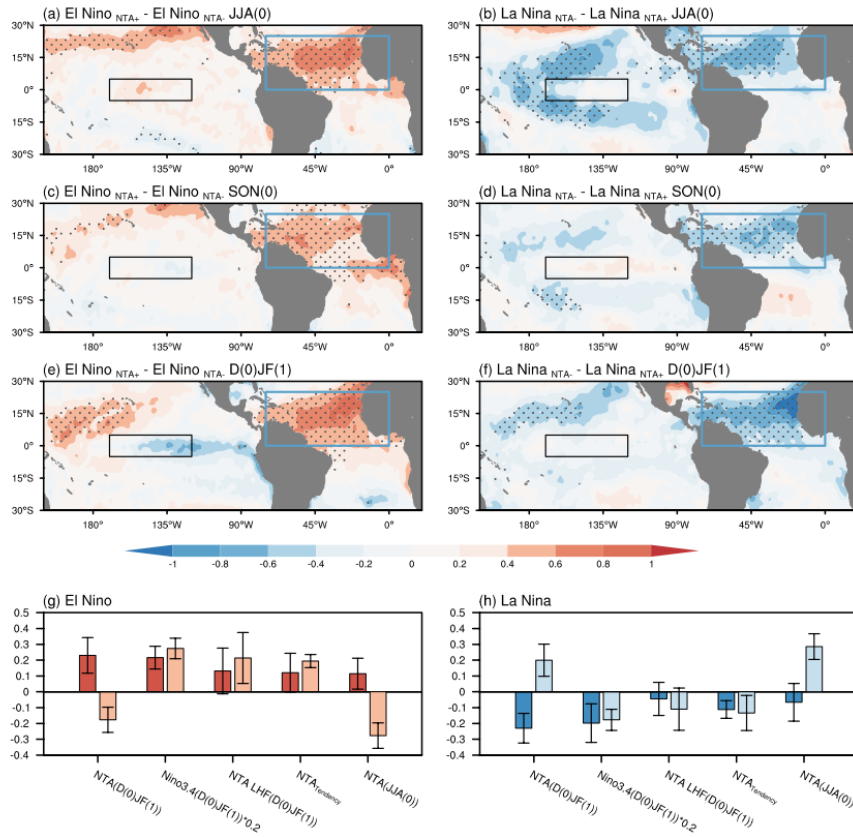


Figure 1. Composite SST anomalies (shading; °C) of El Niño_{NTA+} minus El Niño_{NTA-} events in (a) JJA(0), (c) (SON(0) and (e) D(0)JF(1). (b), (d) and (f), same as (a) (c) and (e) but for La Niña_{NTA+} minus La Niña_{NTA-} events. Dots indicate anomalies that are statistically significant at the 95% confidence level. (g) Composite D(0)JF(1) NTA SST anomalies (°C), D(0)JF(1) Niño3.4 index (°C), D(0)JF(1) latent heat flux (LHF) (°C/3 month) over the NTA, D(0)JF(1) NTA tendency (°C/3 month) and JJA(0) NTA SST anomalies (°C) for El Niño_{NTA+} (dark red bars) and El Niño_{NTA-} (light red bars) events with error bars corresponding to one standard deviation. The composite values for D(0)JF(1) Niño3.4 are scaled by factor of 0.2 for easy comparison. (h) Same as (g), but for La Niña_{NTA+} (light blue bars) and La Niña_{NTA-} (dark blue bars).

8. 约 30 Ma 以来青藏高原向其北缘的脉冲式隆起与生长

翻译人: 张琪 zhangq7@sustech.edu.cn



Wang W, Zhang P, Garzzone C N, et al. *Pulsed rise and growth of the Tibetan Plateau to its northern margin since ca. 30 Ma* [J]. *PNAS*, 2022, 119 (8), e2120364119.

<https://doi.org/10.1073/pnas.2120364119>

摘要: 青藏高原边缘造山运动的开始是制约欧亚大陆地势形成过程的关键因素。尽管加厚地壳的逐渐扩张支撑了大多数模型,但一些研究表明,青藏高原北部更早建立,是在印度和欧亚大陆碰撞后不久(约 50 Ma)形成的。这一推断在很大程度上依赖于柴达木盆地保存下来的新生代沉积物的年代和物源。在此,基于磁地层学和磷灰石碎屑裂变径迹年龄,作者发现高原北部的柴达木盆地起始和演化时间相对较晚,盆地充填时间约为 30 ~ 4.8 Ma。碎屑锆石物源分析与古水流相结合表明,青藏高原东北缘祁连山的发育分别始于约 30 Ma 和 10 Ma。约 30 Ma 和 10 ~ 15 Ma 在青藏高原及其边缘地区广泛存在的同步形变表明,这两个向外生长阶段可能是由于青藏高原不同部位地幔岩石圈的迁移所致。

ABSTRACT: The onset of mountain building along margins of the Tibetan Plateau provides a key constraint on the processes by which the high topography in Eurasia formed. Although progressive expansion of thickened crust underpins most models, several studies suggest that the northern extent of the plateau was established early, soon after the collision between India and Eurasia at ca. 50 Ma. This inference relies heavily on the age and provenance of Cenozoic sediments preserved in the Qaidam basin. Here, we present evidence in the northern plateau for a considerably younger inception and evolution of the Qaidam basin, based on magnetostratigraphies combined with detrital apatite fission-track ages that date the basin fills to be from ca. 30 to 4.8 Ma. Detrital zircon-provenance analyses coupled with paleocurrents reveal that two-stage growth of the Qilian Shan in the northeastern margin of the Tibetan Plateau began at ca. 30 and at 10 Ma, respectively. Evidence for ca. 30 and 10 to 15 Ma widespread synchronous deformation throughout the Tibetan Plateau and its margins suggests that these two stages of outward growth may have resulted from the removal of mantle lithosphere beneath different portions of the Tibetan Plateau.

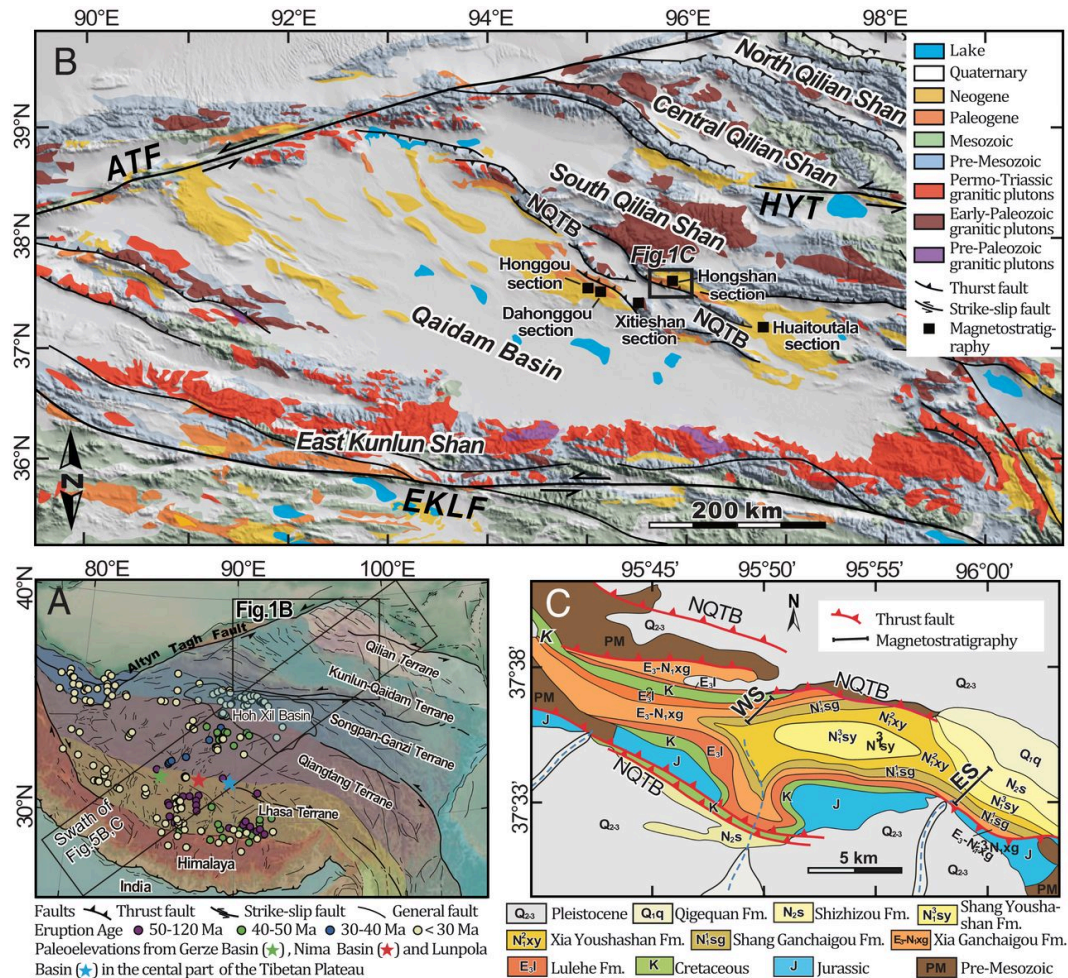


Figure 1. (A) Regional shaded relief map of the Tibetan Plateau showing major faults, terranes, volcanic rock ages, and paleoelevation study sites. The black rectangles outline extent of B and the swath of Fig. 5 B and C. (B) Generalized tectonic and topographic map of the East Kunlun Shan, Qilian Shan, and the Qaidam basin with magnetostratigraphic section locations (solid squares) in the north margin of the basin. ATF, Altyn Tagh fault; EKLF, East Kunlun fault; NQTB, North Qaidam thrust belt; and HYF, Haiyuan fault. (C) Geological map of the Hongshan region [modified after Qinghai Bureau of Geology and Mineral Resources (17)]. Shown are the distributions of Cenozoic stratigraphic units (Lulehe, Xia Ganchaigou, Shang Ganchaigou, Xia Youshashan, Shang Youshashan, Shizigou, and Qigequan formations) in the study area and Hongshan West section (WS) as well as Hongshan East section (ES).

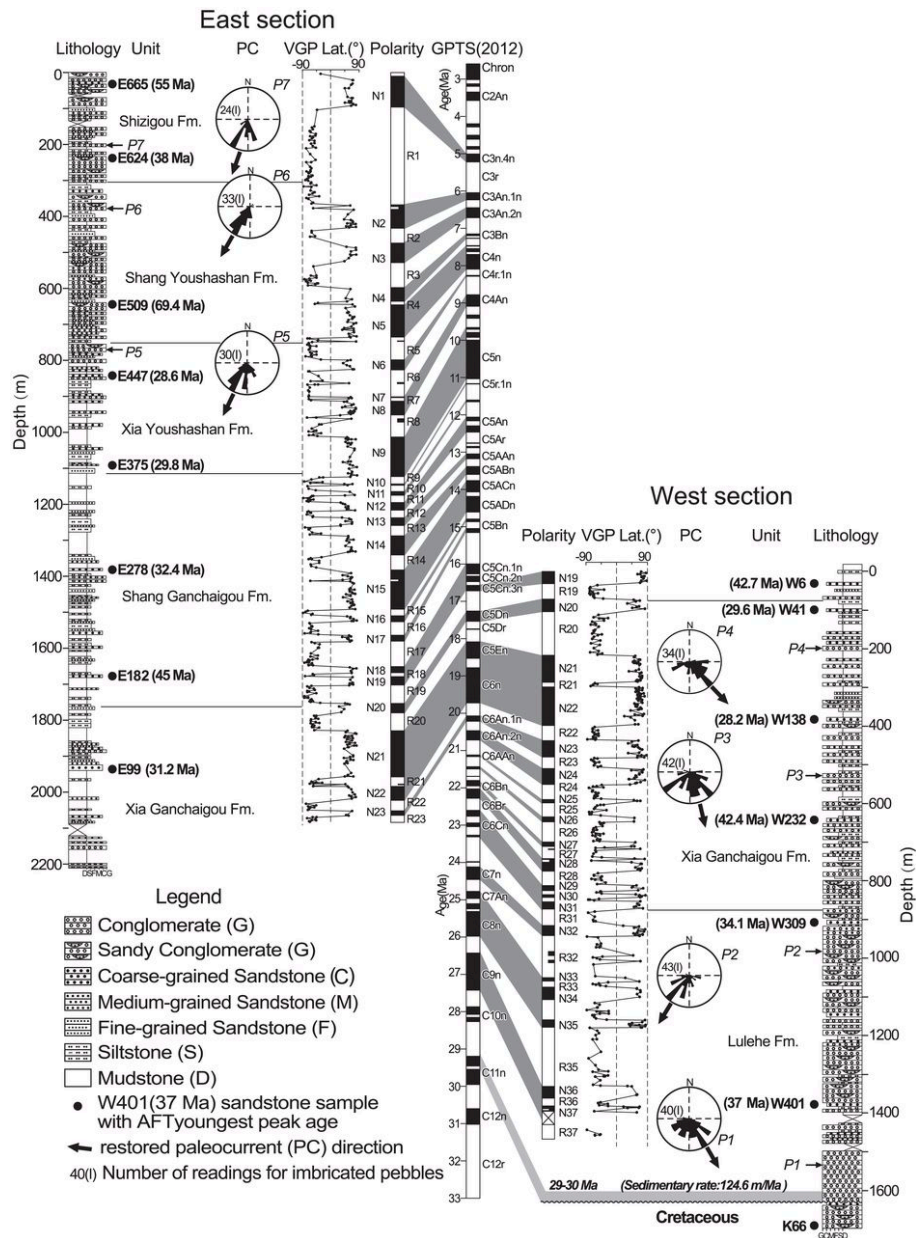


Figure 2. Correlations of observed magnetostratigraphy to the GPTS (2012) (25, 26). Sites of the detrital apatite fission-track samples (with youngest fission-track peak ages), detrital zircon U-Pb samples, and paleocurrent indicators are plotted on the Right or Left of the stratigraphic columns. The youngest peak ages of detrital AFT from basal conglomerates constrained the magnetostratigraphies to younger than 37 Ma.

9. 火星放射性热形成的非岩浆水热系统

翻译人：张伟杰 12031188@mail.sustech.edu.cn



Ojha L, Karunatilake S, Karimi S, et al. *Amagmatic hydrothermal systems on Mars from radiogenic heat*[J]. *Nature communications*, 2021, 12(1): 1-11.

<https://doi.org/10.1029/2021GC010272>

摘要：长期存在的热液系统是火星上天体生物探索的主要目标。与岩浆或撞击环境不同，由于放射性元素(如 U、Th 和 K)的半衰期达到 10 亿年级别，放射性热液系统可以存活上亿年，但其在火星上的存在情况还没有被了解。本文，我们利用地球化学、重力、地形数据和数值模型来寻找火星上潜在的放射性热液系统。我们发现，Eridania 地区曾经有一个巨大的内陆海，其水量可能超过所有其他火星地表水的总和，可能存在放射性热液系统。相比火星上其他地点，Eridania 的放射性热液能够为生命提供更持久的温和条件。放射性热所造成的水的辐射分解能够产生 H₂，成为微生物生命活动中关键的电子供体。此外，热液系统有助于解释该地区的强地壳磁场和重力异常。

ABSTRACT: Long-lived hydrothermal systems are prime targets for astrobiological exploration on Mars. Unlike magmatic or impact settings, radiogenic hydrothermal systems can survive for >100 million years because of the Ga half-lives of key radioactive elements (e.g., U, Th, and K), but remain unknown on Mars. Here, we use geochemistry, gravity, topography data, and numerical models to find potential radiogenic hydrothermal systems on Mars. We show that the Eridania region, which once contained a vast inland sea, possibly exceeding the combined volume of all other Martian surface water, could have readily hosted a radiogenic hydrothermal system. Thus, radiogenic hydrothermalism in Eridania could have sustained clement conditions for life far longer than most other habitable sites on Mars. Water radiolysis by radiogenic heat could have produced H₂, a key electron donor for microbial life. Furthermore, hydrothermal circulation may help explain the region's high crustal magnetic field and gravity anomaly.

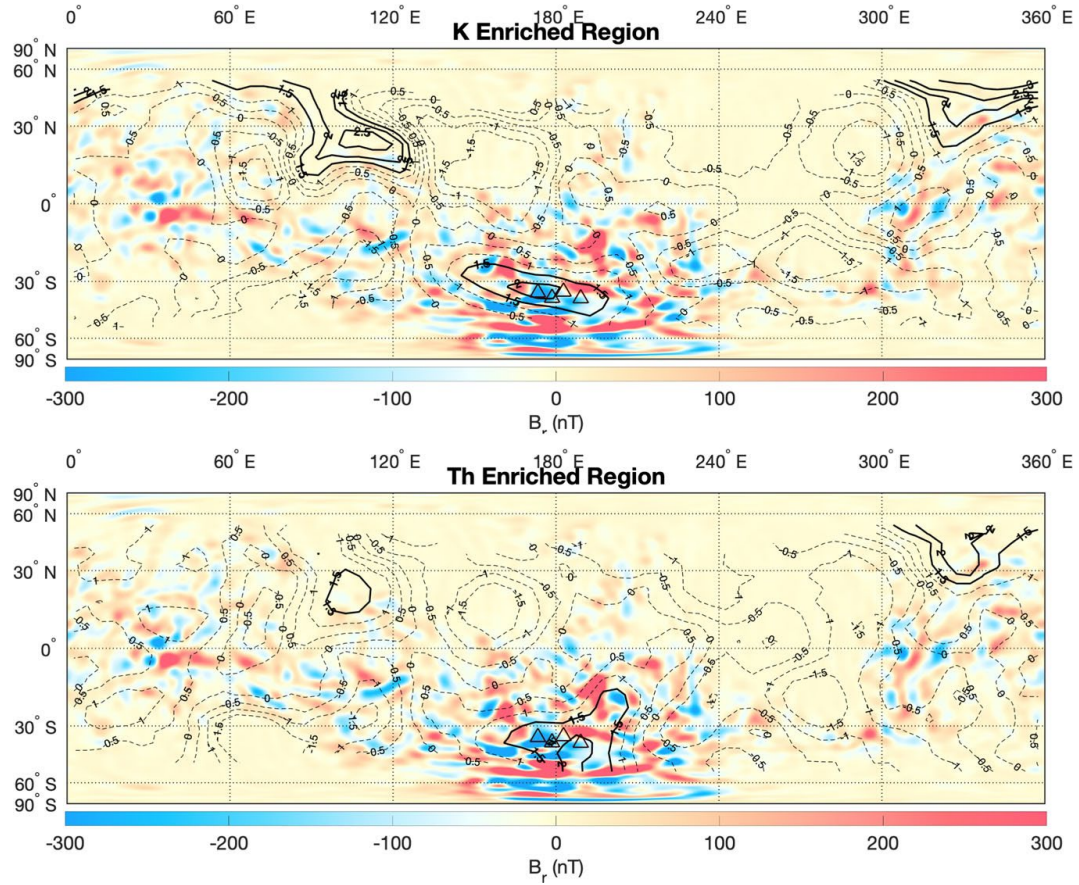


Figure 1. Map of the radial magnetic field of Mars and correlation with elemental K, Th, and Fe. a, K enriched regions on Mars in color overlaid on MOLA shaded relief. The bold black lines show areas on Mars that are statistically enriched in K. The dashed black lines are areas on Mars that have the average K composition or concentration less than the average K composition. b, Same as (a) but for the elemental composition of Th.

10. 青藏高原中部气候变化的轨道驱动揭示了晚渐新世至早中新世 南亚季风的演化

翻译人：曹伟 11930854@qq.com



Su B, Sun J M, Jin C S. Orbital Forcing of Climatic Changes on the Central Tibetan Plateau Reveals Late Oligocene to Early Miocene South Asian Monsoon Evolution [J]. Geophysical Research Letters, 2022, e2021GL097428
<https://doi.org/10.1029/2021GL097428>

摘要：青藏高原的抬升被广泛认为触发了亚洲季风系统。然而，由于青藏高原缺乏长周期高分辨率的古气候记录，南亚季风（SAM）何时到达青藏高原中部尚不清楚。本研究中，我们研究了伦波拉盆地一个湖相层序（约 25.5-19.8 Ma）的环境磁性。赤铁矿是主要的磁性矿物，其浓度随“箱形”峰的变化而变化，这主要是由于在交替的非稳态氧化还原环境中，碎屑氧化铁的优先保存和溶解。环境磁学序列反映了明显的干湿循环，具有~400 kyr 的偏心周期性，这被认为是由 SAM 强度驱动的。因此，我们的研究表明，SAM 增强并向北推进至伦波拉盆地至少在 25.5 Ma。

ABSTRACT: The uplift of the Tibetan Plateau is generally considered to have triggered the Asian monsoon system. However, a long-standing scarcity of high-resolution paleoclimatic records on the Tibetan Plateau makes it unclear when the South Asian monsoon (SAM) reached the central Tibetan Plateau. Here, we investigated the environmental magnetic properties of a lacustrine sequence (~25.5-19.8 Ma) from the Lunpola Basin. Hematite is the dominant magnetic mineral with concentrations that vary with box-shaped peaks that mainly resulted from preferential preservation and dissolution of detrital iron oxides in alternating non-steady-state redox environments. Environmental magnetic sequences reflect distinct dry-wet cycles with a ~400 kyr eccentricity periodicity, which are proposed to have been driven by SAM intensity. Therefore, our study reveals that the SAM intensified and advanced northward to the Lunpola Basin by at least ~25.5 Ma.

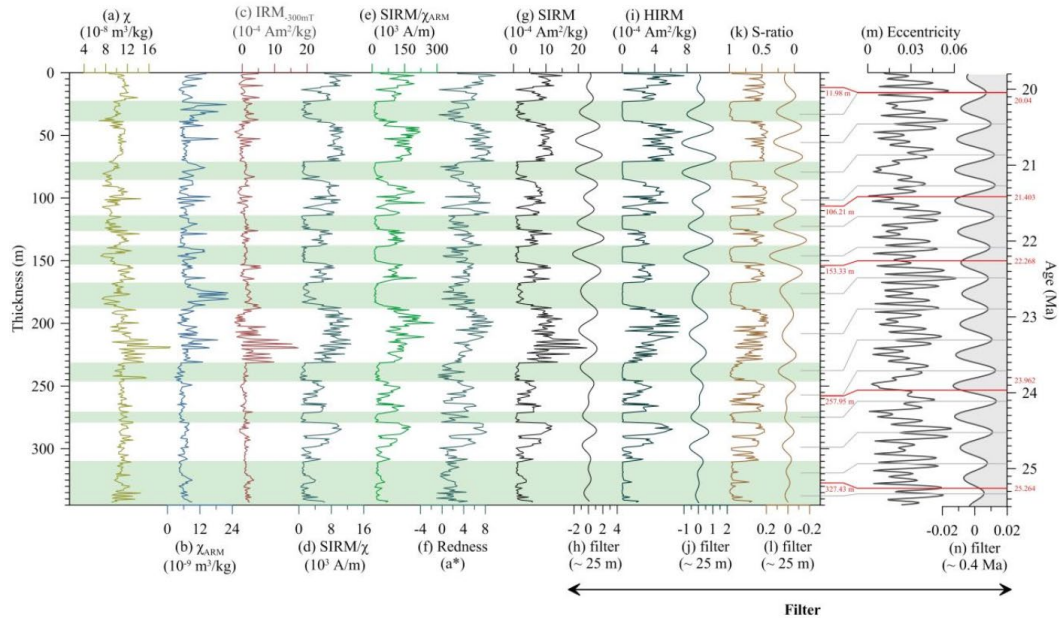


Figure 1. Vertical variation of proxy records, and the comparison between typical proxy sequences and orbital forcing. (a) χ , (b) χ_{ARM} , (c) $\text{IRM}_{300\text{mT}}$, (d) SIRM/χ , (e) $\text{SIRM}/\chi_{\text{ARM}}$, (f) Redness (a^*), (g) SIRM, (h, j, l) ~ 25 m band-pass filter of SIRM, HIRM, and S-ratio, respectively. (i) HIRM, (k) S-ratio, (m) Eccentricity theory curve, La2010d-Ecc3L (Lasker et al., 2011), and (n) ~ 0.4 Ma band-pass filter of eccentricity. The central frequency and bandwidth of ~ 25 m filter and ~ 0.4 Ma filter are 0.041 ± 0.008 cycles/m and 2.469 ± 0.6 cycles/Ma, respectively. The light-green shadows are low-magnetic units, defined by the lower SIRM and HIRM intervals. The red lines represent age control points. Grey lines indicate the periodicity relationship between proxies and eccentricity.

11. 富营养和脱氧驱动 PETM 区间边缘海有机碳埋藏

翻译人：蒋晓东 jiangxd@sustech.edu.cn



Papadomanolaki, N. M., Sluijs, A., Slomp, C. P. Eutrophication and deoxygenation forcing of marginal marine organic carbon burial during the PETM [J]. *Paleoceanography and Paleoclimatology*, (2022). 37, e2021PA004232.

<https://doi.org/10.1029/2021PA004232>

摘要：古新世-始新世极热事件（PETM）是以全球沉积物中有机碳同位素 $\delta^{13}\text{C}$ 负漂作为显著的标志。基于碳同位素漂移，这次事件的起因、持续时间、恢复机制都已被评估。本文我们专注于事件恢复阶段，大陆边缘增强的有机碳埋藏在驱动大气 CO_2 和全球外生 $\delta^{13}\text{C}$ 降低中的作用。新的以及已发表的数据皆表明碳同位素负漂期间，边缘海及受限制的环境内增强的生产力、低氧海水、高有机碳埋藏特征。基于新的地球化学箱式模型对深部以及边缘环境的应用，我们发现大陆边缘海增多的可利用性磷和海水分层能够解释 PETM 期间增强的有机碳埋藏。与现今海洋系统相比，与有机碳相关的脱氧和磷循环非常的温和。我们的模型重复了野外实验，PETM 期间有机碳埋藏超过了古新世时期，达到 6000 亿克，其中 3300 亿克碳是 PETM 恢复期前 40 千年在大陆边缘的沉降。这一结果与先前的模型和数据一致。为重现全球外生 $\delta^{13}\text{C}$ 模式且基于 $\delta^{13}\text{C}$ (-11‰ to -55‰) 的来源，有机碳埋藏暗示在 PETM 前~100-150 千年内注入了 5000-10000 亿吨碳。

ABSTRACT: The Paleocene-Eocene Thermal Maximum (PETM) is recognized globally by a negative excursion in stable carbon isotope ratios ($\delta^{13}\text{C}$) in sedimentary records, termed the carbon isotope excursion (CIE). Based on the CIE, the cause, duration, and mechanisms of recovery of the event have been assessed. Here, we focus on the role of increased organic carbon burial on continental margins as a key driver of CO_2 drawdown and global exogenic $\delta^{13}\text{C}$ during the recovery phase. Using new and previously published sediment proxy data, we show evidence for widespread enhanced primary production, low oxygen waters, and high organic carbon (Corg) burial in marginal and restricted environments throughout the $\delta^{13}\text{C}$ excursion. With a new

biogeochemical box model for deep and marginal environments, we show that increased phosphorus availability and water column stratification on continental margins can explain the increased Corg burial during the PETM. Deoxygenation and recycling of phosphorus relative to Corg were relatively mild, compared to modern day anoxic marine systems. Our model reproduces the conditions reconstructed by field data, resulting in a burial of 6,000 Pg across the PETM, in excess of late Paleocene burial, and ~3,300 Pg C for the critical first 40 kyr of the recovery, primarily located on continental margins. This value is consistent with prior data and model estimates (~2,000–3,000 Pg C). To reproduce global exogenic $\delta^{13}\text{C}$ patterns, this Corg burial implies an injection of 5,000–10,000 Pg C during the first ~100–150 kyr of the PETM, depending on the source's $\delta^{13}\text{C}$ (–11‰ to –55‰).

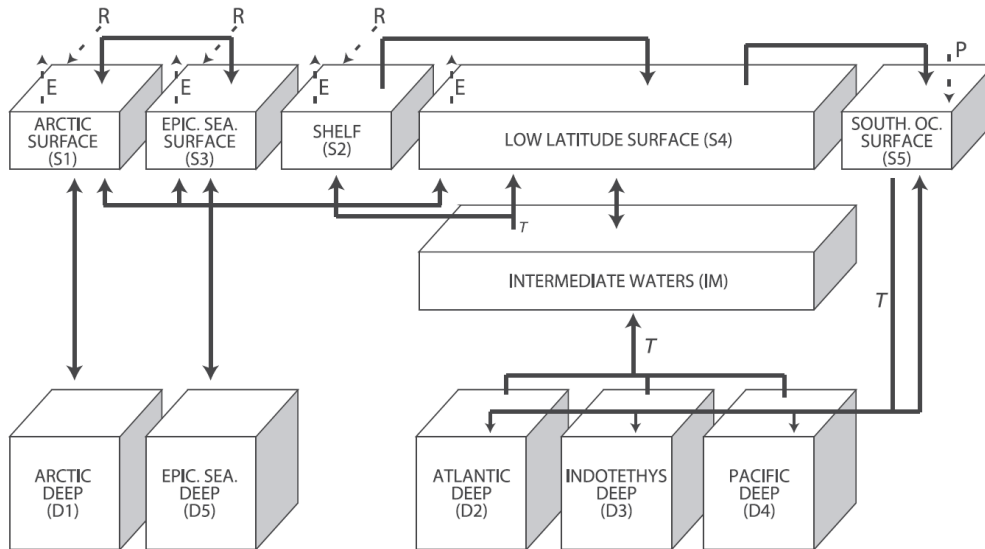
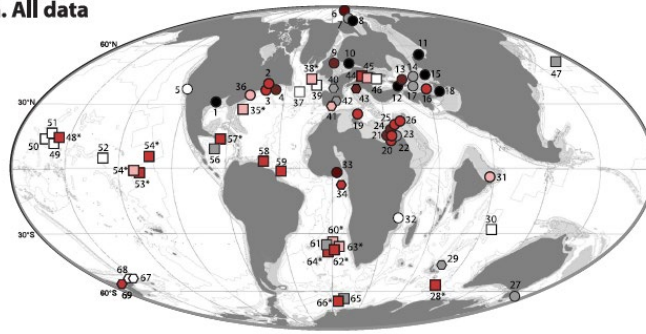


Figure 1. Setup of model boxes with names (codes) and fluxes determining the exchange between them. Fluxes between the boxes are indicated with solid lines and riverine fluxes (R), evaporation (E), and precipitation (P) are indicated by dashed lines. Thermohaline circulation assumes deep water formation in the Southern Ocean (Bice & Marotzke, 2001).

a. All data



b. Recovery only

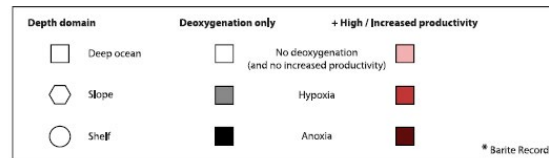
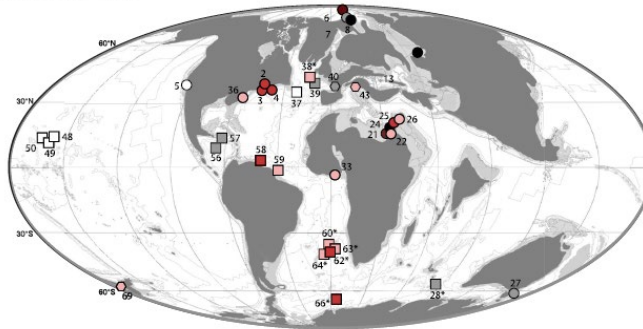


Figure 2. Compilation of maximum sediment Corg contents for the PETM. Colors represent maximum values for each site: less than 0.5 wt % (white), more than 0.5 wt % (gray), and more than 2 wt % (black). Shapes indicate the depth domain: shelf (circle), slope (polygon), and deep (square). For the full reference list and site names (here indicated by numbers) see Table ST1 in Supporting Information S2. Map after Markwick (2007), modified by Sluijs et al. (2014).

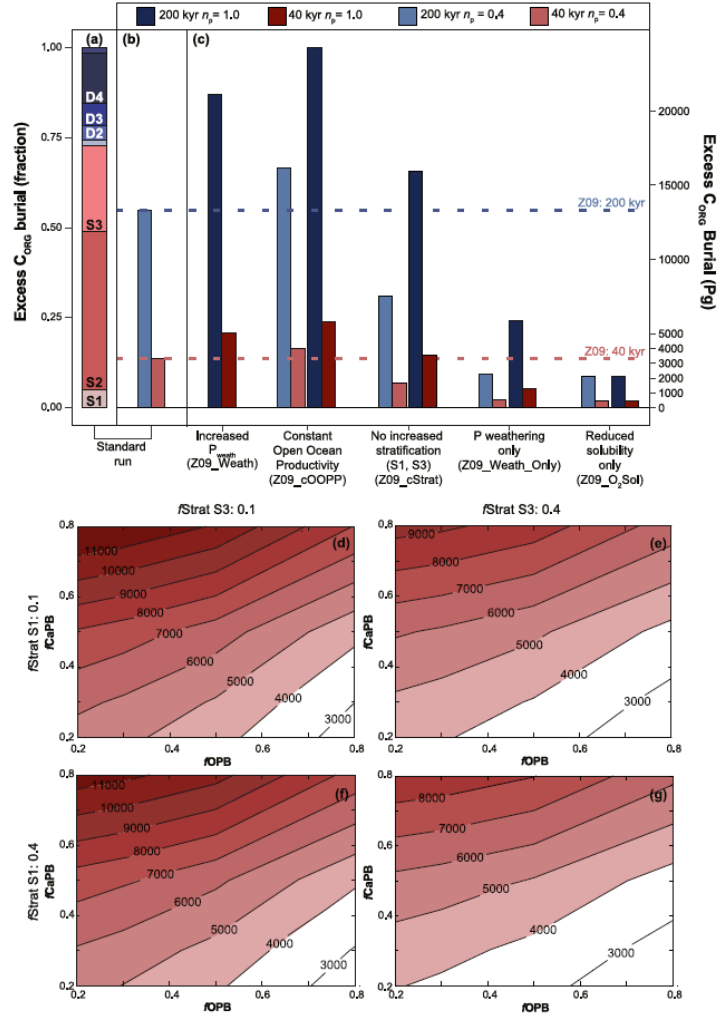


Figure 3. Barplot for excess Corg burial associated with the PETM for the standard simulation Z09 (a, b) and the sensitivity analyses (c) in units of Pg C and as a relative fraction when compared to Z09. The response of Corg burial for the first 40 kyr of the recovery to different degrees of stratification in S1 and S3, as well as varying redox sensitivity for P burial is shown in (d-g). The codes for the boxes contributing to the excess Corg burial are as described in Figure 2. Blue colors are used for excess burial across the entire PETM while red indicates excess burial during the first 40 kyr of the recovery. Light colors in (b, c) are used for the lower P weathering sensitivity ($n_p = 0.4$) while darker shades correspond to the higher sensitivity ($n_p = 1.0$). See the Methods section for an explanation on the calculation of excess burial. Scenario codes are given in brackets and explained in Table ST2 in Supporting Information S2.

12. 全球变暖扰动季风将使东亚气候由干转湿

翻译人: 刘宇星 11811211@mail.sustech.edu.cn



Dai L, Cheng T F, Lu M. Anthropogenic warming disrupts intraseasonal monsoon stages and brings dry-get-wetter climate in future East Asia [J]. Climate and Atmospheric Science, 2022, 5(1).

<https://doi.org/10.1038/s41612-022-00235-9>

摘要: 在气候变暖的情况下, 东亚将面临一个异常的季风周期, 洪水、干旱和天气突变的风险将会陡增。在八个季节内季风阶段框架中, 我们提出了了东亚的“由干转湿”典例, 反驳了“干燥的地方会更干燥, 湿润的地方会更湿润”普遍理论。在时间尺度上, 仲夏和秋季将会延长, 同时伴随着冬季的延迟、缩短和减弱, 尤其在 21 世纪末更是如此。而且整个东亚在春季至仲夏阶段将会经历多达 14-20 天的强降雨。具体而言, 长江流域的洪积期将提前, 洪水风险将不断上升。此外, 黄淮盆地、日本南部和朝鲜半岛的社会安全和生态系统恢复力将遭遇更频繁的极端天气的挑战。在该季风框架下, 一个完整的水气收支解构揭示了降水减缓和“干转湿”模式的原因。。

ABSTRACT: East Asia will face a skewed monsoon cycle with soaring flood, drought, and weather whiplash risks in a warming climate. In our objective eight-intraseasonal-monsoon-stage framework, we uncover a ‘dry-get-wetter’ paradigm in East Asia, contesting the fallen ‘rich-get-richer’ common belief. On timing, the Mid-summer and Fall periods are stretching at the expense of three delayed, shortened, and weakened winter stages, especially near the end of the twenty-first century. On threats, entire East Asia will experience up to 14–20 more heavy precipitation days during the rainy Spring to Mid-summer stages. Specifically, the Yangtze basin will suffer from an earlier pluvial period with escalating flood risks. Moreover, societal security and ecosystem resilience in the Huai-Yellow basin, South Japan, and the Korean Peninsula will be challenged by more frequent weather whiplash. Under the monsoon-stage framework, a complete moisture budget decomposition sheds light on the causes of a slower precipitation scaling and the ‘dry-get-wetter’ paradigm.

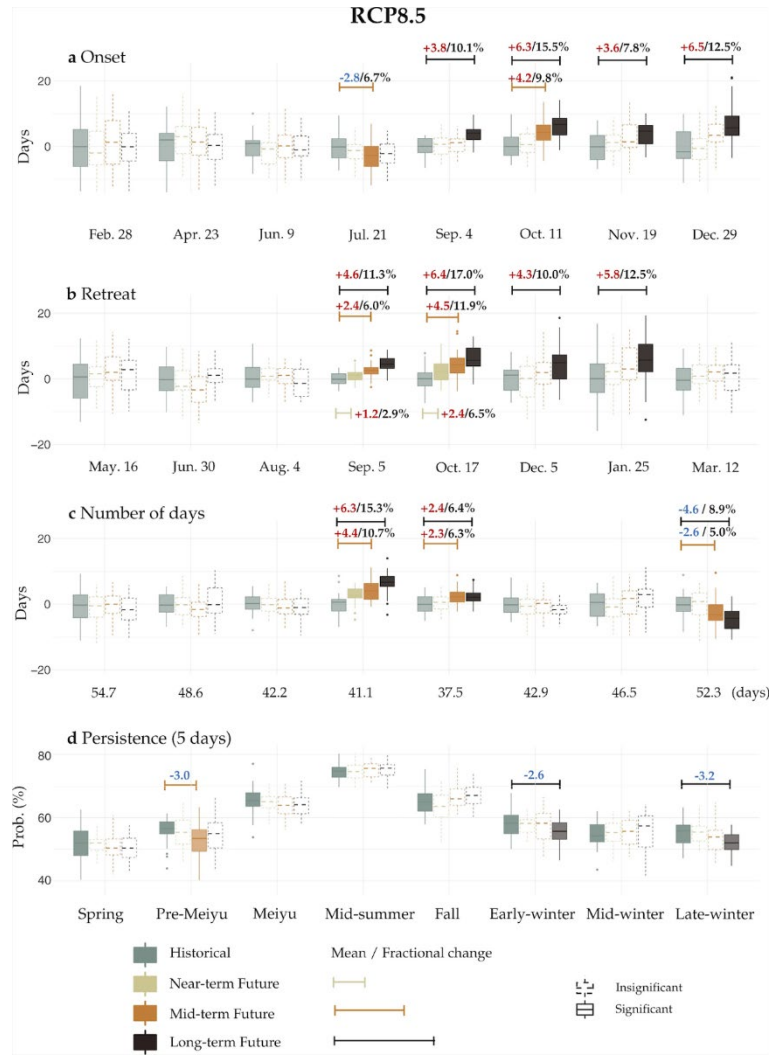


Figure 1. Projected changes in the temporal characteristics of monsoon stages. Boxplots showing interannual variations of a the onset date, b retreat date, c number of days and d the 5-day persistence (see ‘Methods’ for their definitions) of each monsoon stage in the near-term (2011–2040), mid-term (2041–2070), long-term (2071–2100) future compared with historical period (1971–2000) under the RCP8.5 scenario. The historical means of each monsoon stage’s onset date, retreat date and the number of days are provided in the x-axis of the a, b, and c, respectively. A solid boxplot indicates a statistically significant difference between the projected and historical mean at the 0.05 level (Student’s t-test) and is labeled with the corresponding values and fractional changes. The boxplots illustrate the median, the interquartile range, the upper (lower) whisker extending from the hinge to the largest (smallest) value no further than $1.5\times$ interquartile range, and outliers as individual points

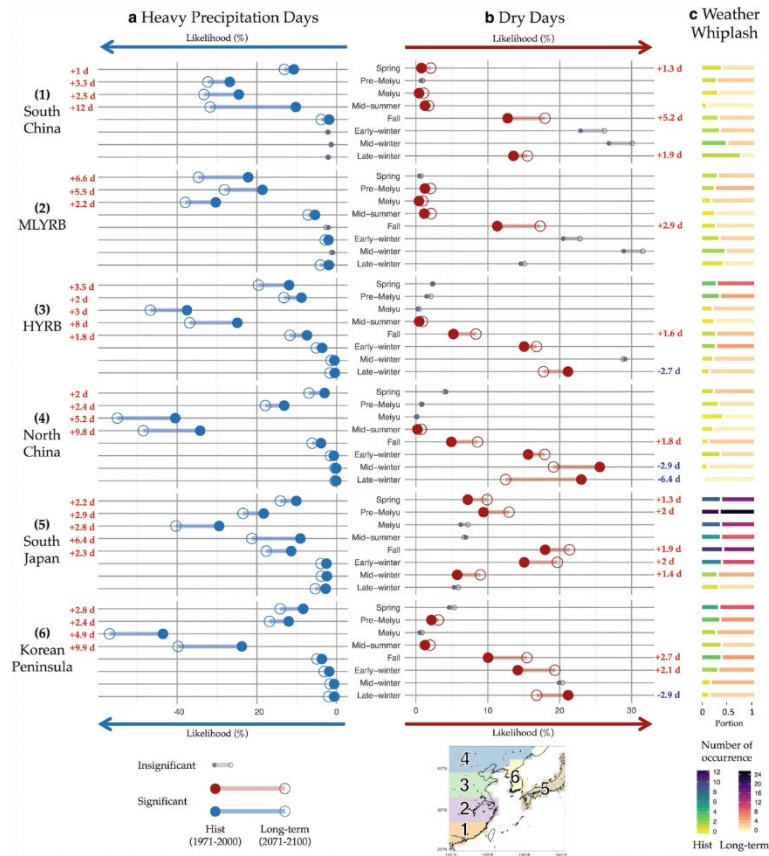


Figure 2. Projected changes in hydrological risks over six East Asian land regions. 30-year averaged multi-model weighted probability of occurrence (or likelihood) (unit: %) of a heavy precipitation days and b dry days during each monsoon stage (see ‘Methods’) under the RCP8.5 scenario. Solid and hollow circles indicate the mean values for the historical period (1971–2000) and the long-term future (2071–2100), respectively. Values significantly different from that of the historical period at the 0.05 level (Student’s t-test) are marked with larger and colored circles; otherwise they are in gray. All significant changes with days greater than one day are labeled. c Bars showing the proportion of the total number of weather whiplash in the historical period (the bar on the left) and in the long-term future (the bar on the right) with respect to their sum. An even split (i.e., 0.5) of the two bars indicates no change in the number of weather whiplash. The colors of the bars show the 30-year averaged multi-model weighted total number of weather whiplash in each period. The changes are shown for all stages in six East Asian land regions: (1) South China, (2) the mid-lower Yangtze River basin (MLYRB), (3) the Huai-Yellow River basin (HYRB), (4) North China, (5) South Japan and (6) the Korean Peninsula.